

# Learning to Pan-sharpening with Memories of Spatial Details

Maoxun Yuan, Tianyi Zhao, Bo Li and Xingxing Wei<sup>‡</sup>

**Abstract**—Pan-sharpening, as one of the most commonly used techniques in remote sensing systems, aims to inject spatial details from panchromatic images into multispectral images (MS) to obtain high-resolution multispectral images. Since deep learning has received widespread attention because of its powerful fitting ability and efficient feature extraction, a variety of pan-sharpening methods have been proposed to achieve remarkable performance. However, current pan-sharpening methods usually require the paired panchromatic (PAN) and MS images as input, which limits their usage in some scenarios. To address this issue, in this paper we observe that the spatial details from PAN images are mainly high-frequency cues, i.e., the edges reflect the contour of input PAN images. This motivates us to develop a PAN-agnostic representation to store some base edges, so as to compose the contour for the corresponding PAN image via them. As a result, we can perform the pan-sharpening task with only the MS image when inference. To this end, a memory-based network is adapted to extract and memorize the spatial details during the training phase and is used to replace the process of obtaining spatial information from PAN images when inference, which is called Memory-based Spatial Details Network (MSDN). Finally, we integrate the proposed MSDN module into the existing deep learning-based pan-sharpening methods to achieve an end-to-end pan-sharpening network. With extensive experiments on the Gaofen1 and WorldView-4 satellites, we verify that our method constructs good spatial details without PAN images and achieves the best performance. The code is available at <https://github.com/Zhao-Tian-yi/Learning-to-Pan-sharpening-with-Memories-of-Spatial-Details.git>.

**Index Terms**—Pan-sharpening, memory-based network, detail injection model, convolutional neural networks.

## I. INTRODUCTION

With the rapid development of spectral imaging technology, multi-spectral (MS) image plays a vital role in many fields [1]–[3], such as climate monitoring, object detection, military reconciliation, and other fields. The significance of remote sensing information is undeniably apparent. For individuals relying on such data, the precision of remote sensing information plays a crucial role in determining the quality of their work and daily life. However, limited by the physical equipment, the onefold sensor cannot guarantee the high spectral and high spatial resolution of the captured images at the same time [4], [5]. Sensors usually obtain either a high-resolution panchromatic (PAN) image or a high-spectral MS

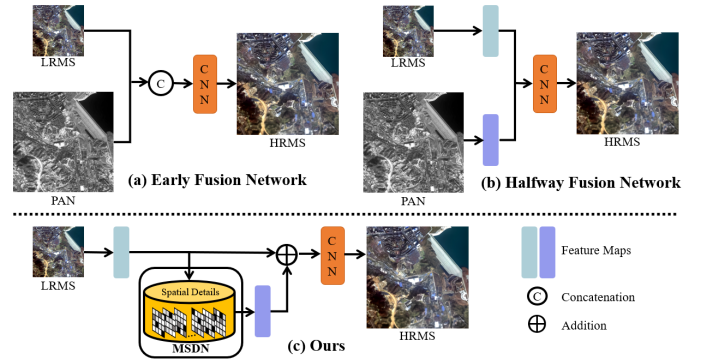


Fig. 1. The comparison between existing DL-based methods and our proposed method. In our approach, PAN image is utilized to supervise the learning process of the memory-based module, while is not required during testing.

image. Therefore, they are usually captured via two different sensors and then fuse a high-resolution multispectral (HRMS) image via pan-sharpening technology [6]–[8]. Thus, the pan-sharpening task can be regarded as a crucial pre-processing step for numerous remote sensing data applications.

Due to the powerful representation ability of convolutional neural network (CNN), many researchers have utilized CNNs for pan-sharpening [9]–[14]. Current deep learning (DL)-based pan-sharpening methods mainly fall into two types: One is the “early fusion” networks [9], [10], [13], [15] as shown in Figure 1-(a), which adopt a pixel-level fusion way to transfer spatial details from PAN image to MS image. Another is the “halfway fusion” networks [12], [16], [17] as shown in Figure 1-(b), which firstly extract the spatial and spectral details from PAN and MS respectively, and then perform interactive fusion process to obtain HRMS images. It is clear that these two kinds of pan-sharpening methods need the paired PAN and MS image as the input. Actually, due to the equipment failure of sensors, the lack of PAN or MS image usually occurs in practise, which will cause these methods to fail. In these scenarios, if we can still perform the pan-sharpening task effectively via only one of the images, it will greatly improve the utilisation of these data and reduce the hardware cost. Several studies [18], [19] consider coloring PAN images to solve the situation where only PAN images are available. While for MS-only situation, a straightforward way is to apply MS super-resolution [20]–[22]. However, the image quality cannot be guaranteed compared to the pan-sharpening methods due to the lack of spatial details from PAN. To this end, this article mainly focuses on pan-sharpening using only MS images.

Maoxun Yuan and Tianyi Zhao are co-first authors. <sup>‡</sup> indicates the corresponding author.

Maoxun Yuan and Bo Li are with the Beijing Key Laboratory of Digital Media, School of Computer Science and Engineering, Beihang University, Beijing 100191, China (email: yuanmaoxun@buaa.edu.cn; boli@buaa.edu.cn).

Xingxing Wei and Tianyi Zhao are with Institute of Artificial Intelligence, Beihang University, Beijing, 100191, China (email: xxwei@buaa.edu.cn; Ty\_Zhao@buaa.edu.cn).

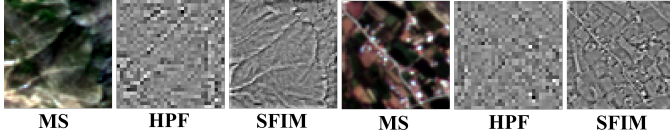


Fig. 2. The visualization of spatial details  $\mathbf{P}_s$  used in DL-based detail injection models. We visualize  $\mathbf{P}_s$  generated from two commonly hand-designed methods (HPF [23] and SFIM [24]).

In fact, pan-sharpening is the process of injecting the spatial details from the PAN image to guide the super-resolution of the MS image. We run some classic main-stream pan-sharpening methods and observe that the extracted spatial details from PAN images are mainly high-frequency cues, i.e., the edges reflect the contour of input PAN images. For example, in Figure 2, we visualize the spatial details extracted by HPF [23] and SFIM [24] algorithms. It can be seen that the spatial details are actually the contour of the PAN image. This motivates us to develop a PAN-agnostic representation to store some base edges, so as to compose the contour of the corresponding PAN image via them. Actually, such a process can be implemented using a memory network [25]. During the training phase, the memory-based network can extract and memorize the spatial details and is supervised by PAN images. In the testing phase, we can utilise the memory-based network to construct spatial details rather than directly obtaining them from the corresponding PAN image. In this way, we can perform the pan-sharpening task only with the MS image when inference and the aforementioned problem are tackled.

To this end, a Memory-based Spatial Details Network (MSDN) is designed to replace the PAN image during testing, as shown in Figure 1-(c). To formulate this network, we decompose it and propose two subnetworks: the memory-controlled subnetwork and the weighted coefficient subnetwork. In the memory-controlled subnetwork, we encode the MS features in the memory encoder to query the corresponding spatial details from the memory bank and then obtain the spatial features through the memory decoder. As for the weighted coefficient subnetwork, we utilize channel attention to predict the weighted features. These two subnetworks are combined to memorize the generation of spatial details during training and construct the required spatial details when inference. To validate the effectiveness of the proposed MSDN, we integrate the proposed MSDN module into the existing DL-based pan-sharpening methods and construct an MSDN-based pan-sharpening framework. To better integrate the MSDN into the framework, we redesign an injection network to inject the generated spatial details adaptively. The overall framework is easy to extend and can be trained in an end-to-end manner.

In summary, our contributions are listed as follows:

- We propose a new way to represent spatial details and perform pan-sharpening task using only MS images. To the best of our knowledge, this is the first attempt to generate the spatial details from a memory network instead of the corresponding PAN image.
- We design a Memory-based Spatial Details Network consisting of a memory-controlled subnetwork and a weighted coefficient subnetwork to generate the required

spatial details from MS features. We also devise a memory-based spatial details learning to memorize the generation of spatial details during training.

- We construct an MSDN-based pan-sharpening framework to assess the effectiveness of MSDN. Extensive experiments on the Gaofen1 and WorldView-4 satellites show that our framework achieves state-of-the-art qualitative and quantitative performance.

The remainder of the article is organized as follows. In the next section, we review the scientific literature related to our proposed approach. Section III presents our motivation and gives a detailed description of the proposed module. Experimental results are presented in Section V, along with a comparison with state-of-the-art methods, and in Section VI we conclude with a discussion of our contribution.

## II. RELATED WORKS

### A. Traditional Spatial Detail Injection Model

The general equation for pan-sharpening detail injection model is as follows:

$$\mathbf{H} = \widetilde{\mathbf{MS}} + g\mathbf{P}_s, \quad (1)$$

where  $\mathbf{H}$  is the predicted HRMS image after pan-sharpening,  $\widetilde{\mathbf{MS}}$  denotes the MS image interpolated at PAN scale,  $g$  represents the injection coefficient that controls the injection of the extracted spatial details and  $\mathbf{P}_s$  indicates the extracted spatial details. The traditional detail injection methods are mainly divided into two kinds of methods: CS-based and MRA-based. The difference between these two methods is manifested mainly in the  $\mathbf{P}_s$  representation of Equation 1.

In the CS-based detail injection model,  $\mathbf{P}_s = (\mathbf{P} - \mathbf{I})$  [4], [26], where  $\mathbf{P}$  is the PAN image and  $\mathbf{I}$  is the intensity component, generally defined as a weighted sum  $\mathbf{I} = \sum_{i=1}^B \omega_i \mathbf{MS}_i$ . On the basis of this expression, many CS-based pan-sharpening algorithms [27], [28] are proposed by exploring different ways to predict the weights  $\omega$  and the injection coefficients  $g$ .

As for the MRA-based detail injection model, the required spatial details  $\mathbf{P}_s$  can be mainly extracted from PAN image,  $\mathbf{P}_s = (\mathbf{P} - \mathbf{P}_l)$  [4], [26], where  $\mathbf{P}_l$  is denoted as the low-pass spatial resolution version of the PAN images. MRA-based methods [29], [30] focus on how to extract the spatial details  $\mathbf{P}_s$  from PAN and estimate the coefficients  $g$ .

### B. DL-based Spatial Detail Injection Model

With the great success of convolutional networks in computer vision tasks, the DL-based detail injection approaches are also proposed in pan-sharpening based on Equation 1. Similar to the traditional methods, the process of some DL-based detail injection methods can be formulated as follows:

$$\mathbf{H} = \widetilde{\mathbf{MS}} + \mathcal{F}_\theta(\mathbf{P}_s), \quad (2)$$

where  $\mathcal{F}_\theta$  is the CNNs with the network parameters  $\theta$ . These methods replace the injection coefficients  $g$  by exploring a non-linear mapping function fed by  $\mathbf{P}_s$ . For example, DiPAN [31] is designed from a general detail injection formulation to

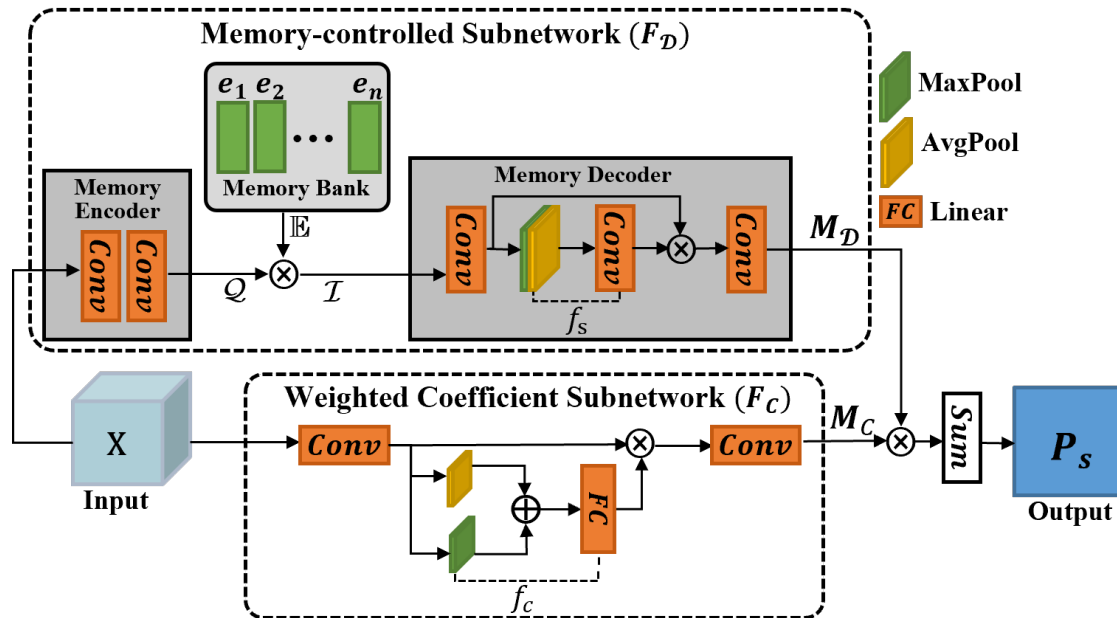


Fig. 3. The overall pipeline of our Memory-based Spatial Details Network.  $\otimes$  and  $\oplus$  denote the operation of the element-wise multiplication and addition respectively. For clear illustration, we do not show the activation functions in this module.

accommodate conventional MRA-based pan-sharpening methods. Similarly, PANNet [32] introduces the high-pass filter [23] into the  $\mathcal{F}_\theta$  to optimize the spatial details into CNNs. Deng et al. [33] develop two detail-based architectures according to Equation 2 called CS-Net and MRA-Net to support injection strategy for CNNs. Recently, DIM-FuNet [34] is proposed to bridge classic models and deep neural networks by integrating detail extraction and injection fidelity terms.

The above DL-based detail injection methods focus on designing successive CNNs architecture to predict injection spatial features  $\mathcal{F}_\theta(\mathbf{P}_s)$  while still using the hand-designed methods to obtain the  $\mathbf{P}_s$  from PAN images. However, this way restricts them must use paired PAN and MS images for pan-sharpening. In this paper, we formulate a new  $\mathbf{P}_s$  representation to solve this problem. Thus, we can use only MS images to perform the pan-sharpening task by representing the overall Equation 2 with CNNs in an end-to-end manner.

### C. Memory networks

Weston et al. [25] first propose memory networks for the task of answering questions. From then on, memory-based networks enter the vision of people. Deng et al. [35] design a long-term memory to memorize the various appearance of objects for video object detection. After that, MGUIT [36] is proposed to store and propagate instance-level style information for image translation. Similarly, Ji et al. [37] present a novel memory-based framework that stores blurry to achieve fine-grained video deblurring. Recently, Yan et al. [38] propose a novel network for pan-sharpening called MMNet, which combines the benefits of both model-based and DL-based methods to enhance the interpretation of the network. Similar to these methods, in this paper, we also propose a memory-based network called MSDN, which is utilized to

replace the traditional hand-designed methods to extract and represent the spatial details  $\mathbf{P}_s$ .

## III. MEMORY-BASED SPATIAL DETAILS NETWORK

In this section, we first introduce our motivation in Section III-A. According to our motivation, we propose the Memory-controlled Subnetwork (Section III-B) and Weighted Coefficient Subnetwork (Section III-C). Finally, we present a Memory-based Spatial Details Learning in Section III-D.

### A. Motivation

As discussed above, the pan-sharpening task can be considered as a process of injecting spatial details of PAN into MS super-resolution. Existing DL-based detail injection models usually rely on traditional hand-designed methods to obtain spatial details. From Figure 2, we can observe that these spatial details obtained from hand-designed methods are mainly high-frequency cues, such as prominent outlines and points. This motivates us whether we can obtain these spatial details generated from the sample-invariant model instead of obtaining them from the corresponding PAN image in DL-based methods. To achieve it, referring to the sparse coding theory [39], [40], we consider utilizing the form of a weighted combination dictionary model to decompose the representation of spatial details  $\mathbf{P}_s$ :

$$\mathbf{P}_s = \sum_{n=1}^N \mathcal{D}_n \mathcal{C}_n = \mathcal{D}\mathcal{C}, \quad (3)$$

where  $\mathcal{D}$  is the spatial dictionary, which needs to be optimized from a large number of spatial detail image patches during training and finally utilized to represent the features of these patches when inference. As for  $\mathcal{C}$ , it is used to sparsely

represent the coefficient of these features. In this way, we can construct the  $\mathbf{P}_s$  for a given PAN image.

### B. Memory-controlled Subnetwork ( $\mathcal{F}_D$ )

To model the spatial dictionary  $\mathcal{D}$ , we consider it is not a simple set of dictionaries but a memory network containing  $N$  slot learnable spatial items. The principle of this memory network  $\mathcal{D}$  is to learn a controller that can dynamically access the relevant spatial features given the upsampled MS features. As shown in Figure 3, the whole subnetwork consists of memory bank, memory encoder, and memory decoder, which are introduced as follows.

**Memory bank.** The memory bank stores the spatial items  $\mathbb{E} = \{e_1, e_2, \dots, e_n\} \in \mathbb{R}^{N \times s^2}$  in the latent embedding space, and each of them is a learnable embedding, where  $s$  is an up-scaling factor. To reduce the size of the memory bank, we fix the dimension of  $\mathcal{E}$  and use the repeat operation to expand it to the required dimension:

$$\mathbb{E} \in \mathbb{R}^{N \times H \times W} = \Gamma_{1 \times H \times W}(\mathbb{E}), \quad (4)$$

where  $\Gamma_{a \times b \times c}(\cdot)$  denotes the  $a \times b \times c$  repeat operations. The weight parameters of the spatial items are initialized with Kaiming initialisation [41] and are updated through the overall training loss of the network.

**Memory encoder.** The memory encoder is utilized to convert the input features into the form of the query features required by the memory bank. Specifically, assuming that the input upsampled MS features are  $\mathbf{X} \in \mathbb{R}^{C \times H \times W}$ , we employ two consecutive convolutional layers to generate the query features. The generation process is defined as:

$$\mathcal{Q} = \mathcal{W}_q * \mathbf{X}, \quad (5)$$

where  $\mathcal{W}_q$  denotes the two consecutive convolutions with kernel sizes  $3 \times 3$  and  $1 \times 1$  respectively. The query feature maps are denoted as  $\mathcal{Q} \in \mathbb{R}^{N \times H \times W}$ .

**Memory decoder.** After obtaining the query features  $\mathcal{Q}$ , we multiply it with the spatial items  $\mathbb{E}$  as input and utilize the memory decoder to extract the spatial features. The input of the memory decoder can be expressed as:

$$\mathcal{I} \in \mathbb{R}^{N \times H \times W} = \mathbb{E} \otimes \mathcal{Q}, \quad (6)$$

where  $\otimes$  is the element-wise multiplication. In the memory decoder, we first acquire a new feature representation by utilizing a  $3 \times 3$  convolution  $\mathcal{W}_c$ . To enrich the representation of spatial features, a spatial attention operation  $f_s$  is deployed to predict the feature weights. Finally, we multiply weights and pass through a  $1 \times 1$  convolution  $\mathcal{W}_d$  to obtain the spatial features  $\mathcal{M}_D \in \mathbb{R}^{C \times H \times W}$ . Formally, the process can be defined as:

$$\mathcal{M}_D = \mathcal{F}_D(\mathcal{I}) = \mathcal{W}_d * ((\mathcal{W}_c * \mathcal{I}) \otimes f_s(\mathcal{W}_c * \mathcal{I})). \quad (7)$$

### C. Weighted Coefficient Subnetwork ( $\mathcal{F}_C$ )

As discussed above, the dictionary  $\mathcal{D}$  is modeled as a memory-based network. To obtain the representation of spatial details  $\mathbf{P}_s$ , we also need to model the sparse coefficient  $\mathcal{C}$ .

Thus, according to the definition of sparse coding in super-resolution [42], we formulate the MS super-resolution as follows:

$$\begin{aligned} \widetilde{\mathbf{MS}} &= \mathcal{D}_l \alpha, \\ \mathbf{H} &= \mathcal{D}_h \alpha, \end{aligned} \quad (8)$$

where  $\alpha$  is the common sparse coefficients,  $\mathcal{D}_l$  and  $\mathcal{D}_h$  are spatial dictionaries extracted from  $\widetilde{\mathbf{MS}}$  and  $\mathbf{H}$ , respectively. According to Equation 8,  $\widetilde{\mathbf{MS}}$  and  $\mathbf{H}$  can deduce each other, as follows:

$$\mathbf{H} = \mathcal{D}_h \mathcal{D}_l^{-1} \widetilde{\mathbf{MS}}, \quad (9)$$

substituting Equation 3 and Equation 9 into Equation 1, we obtain:

$$\begin{aligned} \mathcal{D}_h \mathcal{D}_l^{-1} \widetilde{\mathbf{MS}} &= \widetilde{\mathbf{MS}} + g\mathcal{DC}, \\ g\mathcal{DC} &= (\mathcal{D}_h \mathcal{D}_l^{-1} - 1) \widetilde{\mathbf{MS}}, \\ \mathcal{C} &= \mathcal{D}^{-1} g^{-1} (\mathcal{D}_h \mathcal{D}_l^{-1} - 1) \widetilde{\mathbf{MS}}. \end{aligned} \quad (10)$$

Since  $\mathcal{D}^{-1} g^{-1}$  are the matrix operation and  $(\mathcal{D}_h \mathcal{D}_l^{-1} - 1) \widetilde{\mathbf{MS}}$  can be viewed as the operation of extracting the  $\widetilde{\mathbf{MS}}$  features, the complex representation  $\mathcal{D}^{-1} g^{-1} (\mathcal{D}_h \mathcal{D}_l^{-1} - 1)$  can be solved with CNNs. Specifically, considering the sparse characteristics of  $\mathcal{C}$ , we propose a weighted coefficient subnetwork ( $\mathcal{F}_C$ ) to predict it. In this subnetwork, a channel attention module  $f_c$  is utilized to predict the weighted features, and two  $1 \times 1$  convolutions ( $\mathcal{W}_a$  and  $\mathcal{W}_k$ ) are used to transform the dimensions of the features. Thus, for the input upsampled MS features  $x$ , the output features  $\mathcal{M}_C \in \mathbb{R}^{C \times H \times W}$  can be regarded as the coefficient  $\mathcal{C}$ , which can be represented as:

$$\mathcal{M}_C = \mathcal{F}_C(x) = \mathcal{W}_k * (f_c(\mathcal{W}_a * X) \otimes (\mathcal{W}_a * X)). \quad (11)$$

### D. Memory-based Spatial Details Learning

With the outputs of  $\mathcal{M}_D$  and  $\mathcal{M}_C$ , we perform the element-wise multiplication and then sum over the first dimension to obtain the  $\mathbf{P}_s$ , which can be formulated as:

$$\mathbf{P}_s \in \mathbb{R}^{1 \times H \times W} = \text{Sum}(\mathcal{M}_D \otimes \mathcal{M}_C, \text{dim} = 1). \quad (12)$$

To maintain the sparsity of the output features  $\mathcal{M}_C$ , L1 regularization is used during training to limit the optimization process of  $\mathcal{M}_C$ , which defines as:

$$\mathcal{L}_{norm} = \sum_{i=1}^H \sum_{j=1}^W \sum_{k=1}^C \|\mathcal{M}_{C_{ijk}}\|_1. \quad (13)$$

For the MSDN to memorize the  $\mathbf{P}_s$  generation process through the memory-controlled subnetwork  $\mathcal{D}$  during training, we utilize the high-pass details  $\mathbf{HP}$  [32] computed by subtraction between PAN and low-resolution PAN (obtained by using an averaging filter) as the ground truth to supervise the spatial details learning. To guide the generated  $\mathbf{P}_s$  to be similar to  $\mathbf{HP}$  in their distribution space, we exploit the Kullback-Leibler divergence  $D_{KL}(\cdot)$  to measure and minimise the difference between two distributions. Thus, a spatial details memorizing loss  $\mathcal{L}_{Mem}$  is designed and can be defined as follows:

$$\mathcal{L}_{Mem} = D_{KL}(\mathbf{HP} || \mathbf{P}_s) + \mathcal{L}_{norm}. \quad (14)$$

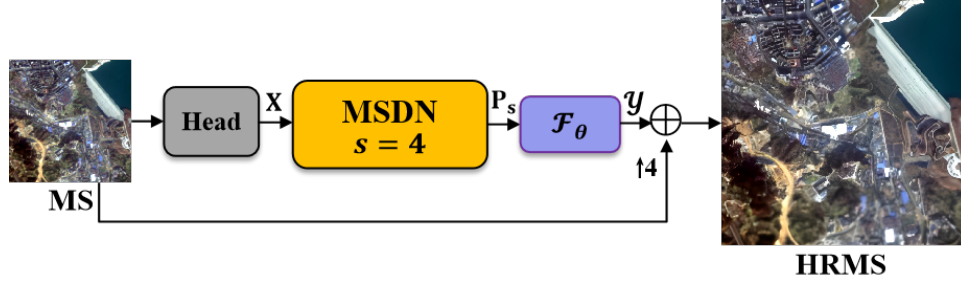


Fig. 4. The architecture of MSDN-based pan-sharpening framework.  $\uparrow$  represents bicubic upsampling operation.

To facilitate the calculation, we stretch two spatial detail features ( $\mathbf{HP}$  and  $\mathbf{P}_s$ ) as vectors. Through the  $\mathcal{L}_{Mem}$  loss, the values of the spatial items are almost constant during training and the generation of spatial details is gradually memorized by the MSDN.

#### IV. MSDN-BASED PAN-SHARPENING FRAMEWORK

To evaluate our MSDN module, we construct a pan-sharpening framework incorporating MSDN. In this framework, we replace the traditional generation process of  $\mathbf{P}_s$  with MSDN and feed the  $\mathbf{P}_s$  into the network  $\mathcal{F}_\theta$  (in Equation 2) to inject spatial features. The detailed descriptions of the framework structure and the loss functions are as follows.

##### A. Overall Framework

As shown in Figure 4, our MSDN works as a plug-in mode and is injected into an existing pan-sharpening framework [33]. In this framework, for the input MS image, stacked residual blocks denoted as *Head* are used to extract MS features. We utilize MSDN after *Head* to replace the original spatial details  $\mathbf{P}_s$  generation:

$$\mathbf{P}_s = \mathcal{F}_{MSDN}(\text{Head}(\text{MS})), \quad (15)$$

where  $\mathcal{F}_{MSDN}$  denotes the MSDN. The generated spatial details  $\mathbf{P}_s$  is then fed into the network  $\mathcal{F}_\theta$  to obtain the injection features  $\mathcal{Y} = \mathcal{F}_\theta(\mathbf{P}_s)$ .

$$\begin{aligned} \mathbf{H} &= \widetilde{\text{MS}} + \mathcal{Y} \\ &= \widetilde{\text{MS}} + \mathcal{F}_\theta(\mathbf{P}_s), \end{aligned} \quad (16)$$

In this framework, we set  $s = 4$  in MSDN to obtain HRMS since the ratio of the spatial resolution between the PAN and the MS is 4. Note that other sizes of HRMS ( $\times 2$  and  $\times 8$ , etc.) can also be generated with our MSDN.

##### B. Re-designed Injection Network

For injection network  $\mathcal{F}_\theta$ , we can use the existing methods to inject the generated  $\mathbf{P}_s$ . To better adapt the MSDN to the framework, we redesign the  $\mathcal{F}_\theta$  and propose the Nested Injection Network (NIN). The structure of the NIN is shown in Figure 5. Since the U-shaped structure [43] performs excellently on the pixel-wise task, we utilize this structure with Injection Block (IB) as a basic block. In IB, each block contains two *PRELU* [41] and three convolutions to improve the feature representation by exploring both positive and

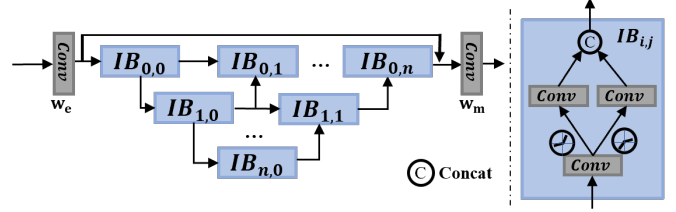


Fig. 5. The flowchart of Nested Injection Network.

negative features. In specific, for the input  $\mathbf{P}_s$ , we first acquire a new feature map  $y_d \in \mathbb{R}^{C \times H \times W}$  by utilizing a convolution layer  $\mathcal{W}_e$ ,  $y_d = \mathcal{W}_e * \mathbf{P}_s$ . To obtain the representation of both positive and negative features, we deploy *PRELU* and convolution layers on  $y_d$  and  $-y_d$  in each block:

$$x_p \in \mathbb{R}^{C/2 \times H \times W} = \mathcal{W}_p * \sigma(y_d), \quad (17)$$

$$x_n \in \mathbb{R}^{C/2 \times H \times W} = \mathcal{W}_n * \sigma(-y_d). \quad (18)$$

where  $\sigma$  denotes the *PRELU* activation,  $\mathcal{W}_p$  and  $\mathcal{W}_n$  are the  $3 \times 3$  convolution layers. We concat  $x_p$  and  $x_n$  together as each output of IB. The final output of NIN can be formulated as:

$$\mathcal{Y} \in \mathbb{R}^{4 \times H \times W} = y_d + \mathcal{W}_m * f_{IB}(y_d), \quad (19)$$

where  $f_{IB}$  represents the U-shaped IB group and  $\mathcal{W}_m$  is the final  $1 \times 1$  convolution layer.

##### C. Loss Functions

As mentioned above, the overall loss function consists of two parts: one is the mean absolute error loss ( $\mathcal{L}_1$ ) aims at reconstructing the HRMS image with the ground-truth MS image and the other is the spatial details memorizing loss ( $\mathcal{L}_{Mem}$ ) which is used to supervise MSDN to reconstruct spatial details  $\mathbf{P}_s$ . The final loss function of our framework is written as follows:

$$\begin{aligned} \mathcal{L}_1 &= \|\mathbf{H} - \text{GT}\|_1, \\ \mathcal{L} &= \mathcal{L}_1 + \lambda \mathcal{L}_{Mem}, \end{aligned} \quad (20)$$

where  $\mathbf{H}$  is the predicted HRMS,  $\text{GT}$  is the ground-truth HRMS and  $\lambda$  is a hyper-parameter for balancing ( $\mathcal{L}_1$ ) and ( $\mathcal{L}_{Mem}$ ) loss functions. In our setting,  $\lambda$  is set as 0.001, such that the average gradient of each loss is at the same scale.

TABLE I  
DESCRIPTION OF THE PAN-SHARPENING QUALITY METRICS.

Metrics	Full name	Formula	Nomenclature
ERGAS	Erreur Relative Global Adimensionnelle de Synthèse	$ERGAS = 100 \cdot \frac{h}{l} \sqrt{\frac{1}{K} \sum_{k=1}^K \left( \frac{RMSE(X_k, Y_k)}{E[X_k]} \right)^2}$ $RMSE(X, Y) = \sqrt{E[(X - Y)^2]}$	$X$ : : the predicted fused images; $Y$ : the reference image; $X'$ : the weighted sum of each band of MS image; $Y'$ : the weighted sum of each band of PAN image; $K$ : the number of image channels; $E[\cdot]$ : the average value of all pixel; $\mathcal{L}$ : the Laplace operator; $h$ : spatial resolutions of PAN image; $l$ : the spatial resolutions of MS image; $\sigma$ : the standard deviation; $\mu$ : the mean value; $\ \cdot\ $ : $L_2$ normalization; $\langle \cdot, \cdot \rangle$ : the inner product.
SAM	Spectral Angle Mapper	$SAM(X, Y) = E \left[ \arccos \left( \frac{\sum_{k=1}^K \langle X_k, Y_k \rangle}{\ X_k\ _2 \cdot \ Y_k\ _2} \right) \right]$	
SCC	Spatial Correlation Coefficient	$SCC = \frac{E[(\mathcal{L} * X - \mu_{X'}) (\mathcal{L} * Y - \mu_{Y'})]}{\sqrt{E[(\mathcal{L} * X - \mu_{X'})^2] E[(\mathcal{L} * Y - \mu_{Y'})^2]}}$	
Q4	Unique Score index Q4 for 4-band MS images	$Q4 = Q(X', Y') = \frac{\sigma_{X'Y'}}{\sigma_{X'} \sigma_{Y'}} \cdot \frac{2 \mu_{X'} \mu_{Y'}}{\mu_{X'}^2 + \mu_{Y'}^2} \cdot \frac{2 \sigma_{X'} \sigma_{Y'}}{\sigma_{Y'}^2 + \sigma_{X'}^2}$	
QNR	Quality with No-Reference	$QNR = (1 - D_\lambda)^\alpha (1 - D_S)^\beta$	$\mathbf{P}$ : the original PAN images; $\mathbf{P}_l$ : the low-pass spatial resolution of PAN images; $p$ : the coefficient to enhance the spectral differences; $q$ : the coefficient to enhance the spatial differences; $d_{i,j}(\mathbf{MS}, \mathbf{H}) = Q(\mathbf{MS}_i, \mathbf{MS}_j) - Q(\mathbf{H}_i, \mathbf{H}_j)$ ; $\alpha$ and $\beta$ : hyperparameter, usually set to 1.
$D_\lambda$	Spectral Distortion Index	$D_\lambda = \sqrt[p]{\frac{1}{K(K-1)} \sum_{i=1}^K \sum_{j=1, j \neq i}^K  d_{i,j}(\mathbf{MS}, X) ^p}$	
$D_s$	Spatial Distortion Index	$D_s = \sqrt[q]{\frac{1}{K} \sum_{i=1}^K  Q(X_i, \mathbf{P}) - Q(\mathbf{MS}_i, \mathbf{P}_l) ^q}$	

TABLE II

ABLATION EXPERIMENTS FOR COMPONENTS IN OUR FRAMEWORK ON THE GAOFEN1 DATASET. THE BEST RESULTS ARE HIGHLIGHTED IN **BOLD**.

MSDN	NIN	SAM↓	ERGAS↓	SCC↑	Q4↑
		0.117	7.530	0.886	0.658
✓		0.102	6.607	0.906	0.703
✓	✓	<b>0.099</b>	<b>6.320</b>	<b>0.912</b>	<b>0.705</b>

TABLE III

ABLATION EXPERIMENT FOR THE SIZES OF THE MEMORY BANK ON THE GAOFEN1 DATASET. THE BEST RESULTS ARE HIGHLIGHTED IN **BOLD**.

Size N	SAM↓	ERGAS↓	SCC↑	Q4↑
<b>16</b>	0.101	6.331	0.910	0.703
<b>32</b>	0.100	6.400	0.911	0.703
<b>64</b>	<b>0.099</b>	<b>6.320</b>	<b>0.912</b>	<b>0.705</b>
<b>128</b>	0.100	6.422	0.908	0.699

## V. EXPERIMENTS

In this section, we first describe the datasets and evaluation metrics used in our experiments. Then, an exhaustive investigation of ablation studies is presented. Next, we visualize the intermediate results of our method. Finally, to illustrate the effectiveness of our method, comparison experiments were conducted with some closely related methods at reduced resolution data and full resolution data, respectively. Moreover, since our method only requires MS image during in the inference like the MS image super-resolution method, we additionally conduct comparison experiments with the promising super-resolution method to illustrate the effectiveness of the method from the side.

### A. Datasets and Metrics

**Datasets.** In this work, all the experiments are conducted on the released pan-sharpening datasets [44], where each satellite includes urban, green vegetation, water scenario, and unlabelled with mixed feature data. We choose Gaofen-1

and WorldView-4 satellites for the experiments. For Gaofen1, the spatial resolution of the PAN images and MS images is 2m and 8m, respectively. For WorldView-4, the spatial resolutions of PAN images and MS images are 0.31m and 1.24m, respectively. In both datasets, the initial sizes of the PAN and MS images are  $1024 \times 1024 \times 1$  and  $256 \times 256 \times 4$ . In order to obtain more training samples, we crop them into image patches of size  $256 \times 256 \times 1$  and  $64 \times 64 \times 4$  and take these as original images. The MS bands are composed of four standard colors (RGB and near-infrared). Following the Wald's protocol [45], the PAN images and the MS images are downsampled by a low-pass filter into image patches of size  $64 \times 64 \times 1$  and  $16 \times 16 \times 4$ , respectively. Furthermore, they are divided into the training set with 90% pairs and the test set with 10% pairs, and the original MS images with a size of  $64 \times 64 \times 4$  are used as the ground truth.

**Metrics.** The performance assessment is conducted both at reduced and full resolution. For the reduced-resolution, five commonly used evaluation metrics are adopted for evaluating

TABLE IV  
ABLATION EXPERIMENT FOR THE DEPTH OF NIN LAYERS IN OUR FRAMEWORK. THE BEST RESULTS ARE HIGHLIGHTED IN **BOLD**.

Depth of NIN	SAM↓	ERGAS↓	SCC↑	Q4↑
1	0.101	6.371	0.908	0.702
2	0.100	6.333	0.911	0.703
3	<b>0.099</b>	<b>6.320</b>	<b>0.912</b>	<b>0.705</b>
4	<b>0.099</b>	6.365	0.910	0.699

TABLE V  
QUANTITATIVE RESULTS TO VERIFY THE VERSATILITY OF MSDN.

×2	×4	SAM↓	ERGAS↓	SCC↑	Q4↑
	✓	0.099	6.320	0.912	0.705
✓	✓	<b>0.098</b>	<b>6.293</b>	<b>0.913</b>	<b>0.706</b>

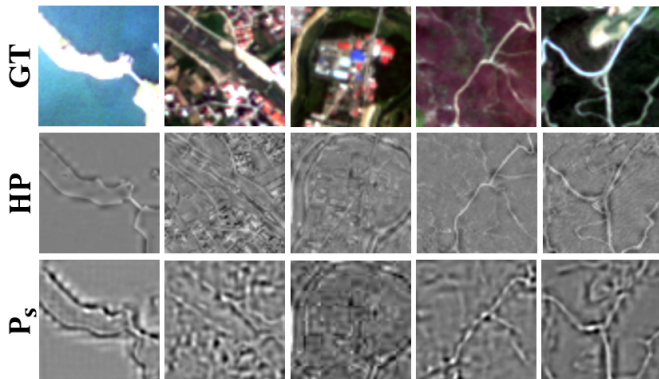


Fig. 6. Visualization of generated spatial details  $P_s$ . HP is the high-pass images extracted from PAN images.

the fusion performance, including SCC [46], ERGAS [28], SAM [47] and Q4 [48]. For the full-resolution, since there are no GT images to assess the performance, we apply QNR,  $D_\lambda$  and  $D_s$  indexes [49] for the quality evaluation. The detailed information is presented in Table I.

### B. Implementation details and Benchmarks

**Implementation details.** For a fair comparison, all experiments are conducted on a single Nvidia GTX 2080Ti GPU and the same Pytorch [50] environments with 12GB memory. During training, our methods optimized by Adam [51] optimizer over 200 epochs with a batch size of 16. Horizontal and vertical flipping are also adopted for data augmentation. The learning rate is initialized with  $4 \times 10^{-4}$  and decayed by multiplying 0.5 when reaching 50 epochs. For other comparison methods, we apply the default settings in related papers and codes. During inferencing, our method accomplishes the pan-sharpening task without PAN images.

**Benchmarks.** We compare our method with several representative state-of-the-art methods. For pan-sharpening: Four CS-based methods, GS [52], GSA [53], Brovey [54] and GFPCA [55]; Three MRA-based methods: SFIM [24], MTF-GLP [29]

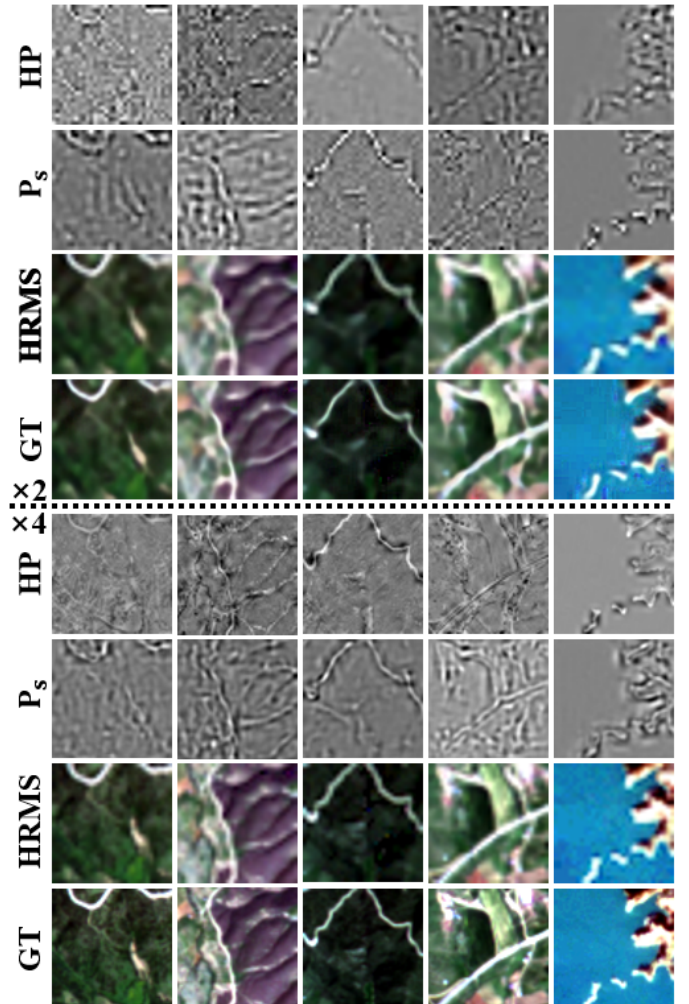


Fig. 7. Multiscale Outputs visualization.  $\times 2$  indicate double up-sampling ( $16 \times 16 \rightarrow 32 \times 32$ ) and  $\times 4$  indicate quadruple up-sampling ( $16 \times 16 \rightarrow 64 \times 64$ ).

and MTF-GLP-HPM [56]; Five DL-based methods: PNN [9], PANNet [32], MSDCNN [57], FusionNet [33] and ADKNet [58]. As for remote sensing Super-Resolution: Five DL-based methods, SRCNN [20], VDSR [59], LGCNet [60], DCM [21] and HSENet [22].

### C. Ablation experiments

**Ablation on our framework.** We ablate the components in our constructed framework to investigate the effectiveness of these designs. The baseline is our framework without MSDN and  $\mathcal{F}_\theta$ . From Table II, each metric has been improved after adding the proposed MSDN. These metrics show that it is feasible to obtain spatial details generated from the memory-based network. These metrics are further improved by adding NIN to our framework, which demonstrates the significance of NIN.

**Size of the memory bank.** We also conduct experiments to demonstrate the impact of the N size of the memory bank in the MSDN. In the experiments, we modify N to  $N = \{16, 32, 64, 128\}$ . The results are shown in Table III. We observe that better pan-sharpening performance can be

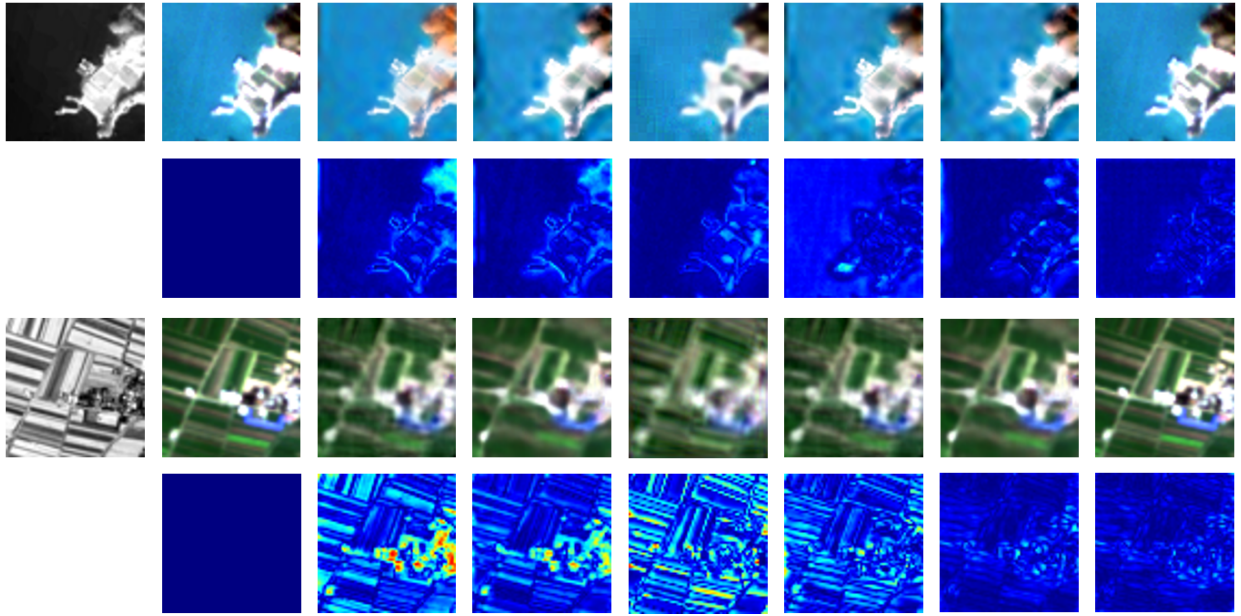


Fig. 8. Visual results generated by different typical pan-sharpening methods. From left to right: PAN, Ground-Truth (GT), Brovey, MTF-GLP-HPM, PANNet, FusionNet, ADKNet and Ours. MAE denotes the (normalized) mean absolute error across all spectral bands.

achieved by increasing the sizes from 16 to 64. However, performance gets worse as the size increases to 128.

**Depth of NIN.** To explore the impact of depth of NIN, we experiment with various depths. In Table IV, we can see that better pan-sharpening performance can be achieved by increasing the layers from 1 to 3. However, continuing to increase the depth can not improve the performance but add computational complexity. Therefore, in our implementation, we choose the 3 depths of NIN.

#### D. Visualization of Spatial Details

To illustrate the effectiveness of our proposed MSDN, we visualize the spatial details generated  $P_s$  in different scenes including urban areas, green vegetation, and water scenarios. As shown in Figure 6, we can find that the generated  $P_s$  is close to the **HP** extracted from the PAN images. From the second and third columns in Figure 6, although the scene is complex, MSDN can still generate spatial details similar to **HP**. All results demonstrate that MSDN has great generation ability.

#### E. Discussion of Multiscale Outputs

As mentioned in subsection IV-A, our MSDN can generate different upscaled sizes of spatial details  $P_s$ . To illustrate its versatility, we stack the MSDN and extend the framework to the multiscale framework. Thus, different upscaled sizes of HRMS can also be predicted. From Table V and Figure 7, we can see that the multiscale framework further improves all the metrics and the different upscaled outputs are close to their corresponding GT images. The above results verify the versatility of our MSDN.

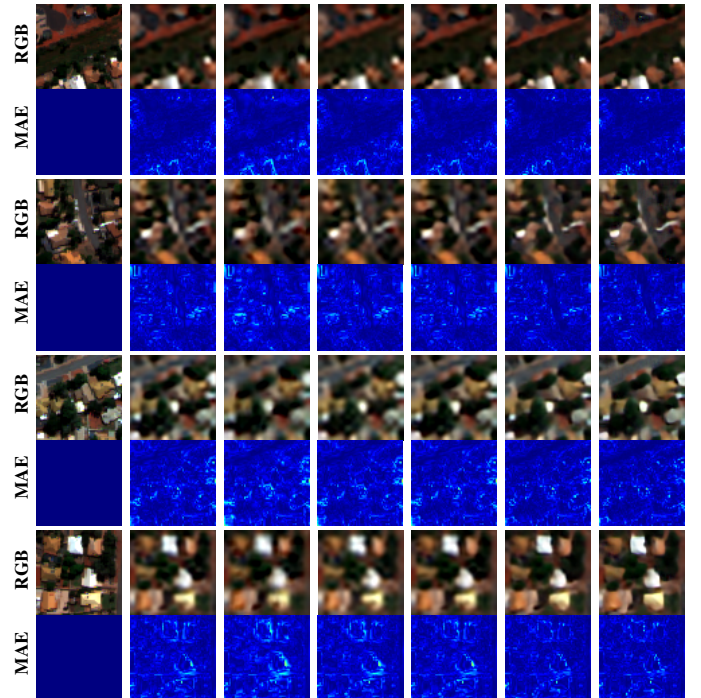


Fig. 9. Visualization results generated by different super-resolution methods (left to right: Ground-Truth (GT), SRCNN [20], VDSR [59], DCM [21], LGCNet [60], HSENet [22] and Ours). MAE denotes the (normalized) mean absolute error across all spectral bands.

#### F. Pan-sharpening on reduced-resolution scene

**Quantitative comparison.** The quantitative comparison results over Gaofen1 and WorldView-4 satellite datasets are reported in Table VI, where the best results are highlighted in bold. As shown in Table VI, although our method performs pan-sharpening without PAN image in the testing phase, the



TABLE VI

QUANTITATIVE COMPARISON ON THE GAOFEN-1 AND WORLDVIEW-4 DATASET AT REDUCED-RESOLUTION. VALUES ARE KEPT TO THREE DECIMAL PLACES. THE UP- OR DOWN-ARROW INDICATES THAT HIGHER OR LOWER METRIC CORRESPONDS TO BETTER IMAGES. THE BEST RESULTS ARE HIGHLIGHTED IN **BOLD**.

Methods	GaoFen-1				WorldView-4			
	SAM↓	ERGAS↓	SCC↑	Q4↑	SAM↓	ERGAS↓	SCC↑	Q4↑
GS [52]	0.213	13.933	0.732	0.512	0.213	9.379	0.682	0.521
GSA [53]	0.187	10.534	0.825	0.539	0.210	7.878	0.685	0.515
Brovey [54]	0.183	14.041	0.764	0.567	0.206	8.689	0.706	0.544
GFPCA [55]	0.182	11.163	0.819	0.571	0.205	7.807	0.725	0.563
SFIM [24]	0.181	13.281	0.813	0.610	0.198	7.623	0.736	0.569
MTF-GLP [29]	0.191	11.964	0.818	0.623	0.187	6.960	0.753	0.588
MTF-GLP-HPM [56]	0.192	10.276	0.782	0.636	0.189	7.063	0.778	0.597
PNN [9]	0.144	8.509	0.875	0.640	0.173	6.495	0.843	0.628
PANNet [32]	0.137	8.569	0.880	0.647	0.166	6.827	0.845	0.644
MSDCNN [57]	0.135	8.215	0.883	0.657	0.156	6.606	0.845	0.648
FusionNet [33]	0.133	8.179	0.890	0.665	0.176	6.198	0.853	0.668
ADKNet [58]	0.119	7.670	0.894	0.674	0.144	5.827	0.877	<b>0.673</b>
Ours	<b>0.099</b>	<b>6.320</b>	<b>0.912</b>	<b>0.705</b>	<b>0.125</b>	<b>5.681</b>	<b>0.879</b>	0.654

TABLE VII

QUANTITATIVE COMPARISON ON THE WORLDVIEW-4 DATASET WITH MS IMAGE SUPER-RESOLUTION METHODS. THE BEST RESULTS ARE HIGHLIGHTED IN **BOLD**.

Methods	SAM↓	ERGAS↓	SCC↑	Q4↑
SRCNN [20]	0.140	6.909	0.824	0.531
VDSR [59]	0.144	6.883	0.828	0.539
DCM [21]	0.148	7.139	0.816	0.515
LGCNet [60]	0.142	7.018	0.823	0.525
HSENet [22]	0.136	6.397	0.845	0.564
Ours	<b>0.125</b>	<b>5.681</b>	<b>0.879</b>	<b>0.654</b>

performance of our framework still surpasses the other promising pan-sharpening methods. Furthermore, through the SAM and ERGAS metrics, we can observe that our results preserve more spectral information due to the absence of PAN image features. Meanwhile, our method also achieves competitive results on spatial metric SCC. The above results well prove the effectiveness of our method, which only uses MS image for pan-sharpening while ensuring the sharpening performance.

**Qualitative comparison.** We also show the qualitative comparison of the visual results to prove the effectiveness of our method. We randomly select images from the GaoFen1 and WorldView-4 datasets to present the RGB channel of output results as shown in Figure 8. The mean absolute error (MAE) is used to calculate the difference between the outputs and the ground truth. Compared with the other pan-sharpening methods, our method has a higher coincidence with the ground truth, which demonstrates that our model has minor spatial

TABLE VIII

THE NON-REFERENCE METRICS ON THE WORLDVIEW-4 DATASET AT FULL-RESOLUTION. BEST RESULTS HIGHLIGHTED IN **BOLD**.

Methods	QNR↑	D <sub>s</sub> ↓	D <sub>λ</sub> ↓
PNN [9]	0.736	0.161	0.131
PANNet [32]	0.739	0.159	0.129
MSDCNN [57]	0.745	0.174	0.122
FusionNet [33]	0.759	0.128	0.128
ADKNet [58]	0.757	0.145	0.121
Ours	<b>0.812</b>	<b>0.115</b>	<b>0.086</b>

and spectral distortions. In general, these visualisation results further testify to the superiority of MSDN in spectral and spatial fidelity.

### G. Comparisons with MS image super-resolution methods

**Quantitative comparison.** Since our method only requires the MS image in the inference phase like the super-resolution method, we additionally conduct comparison experiments with other promising super-resolution methods of the MS image to illustrate the effectiveness of the method from the side. As shown in Table VII, obviously, despite performing well on spectral metrics SAM and ERGAS, super-resolution methods are inferior to pan-sharpening methods on the spatial metric SCC due to the lack of PAN images. However, our method achieves 0.879 on SCC while also obtaining the highest score on the spectral metrics, which verifies its effectiveness in improving the spatial resolution of super-resolution methods.

**Qualitative comparison.** We also visualize super-resolution images for comparison with other methods. As shown in

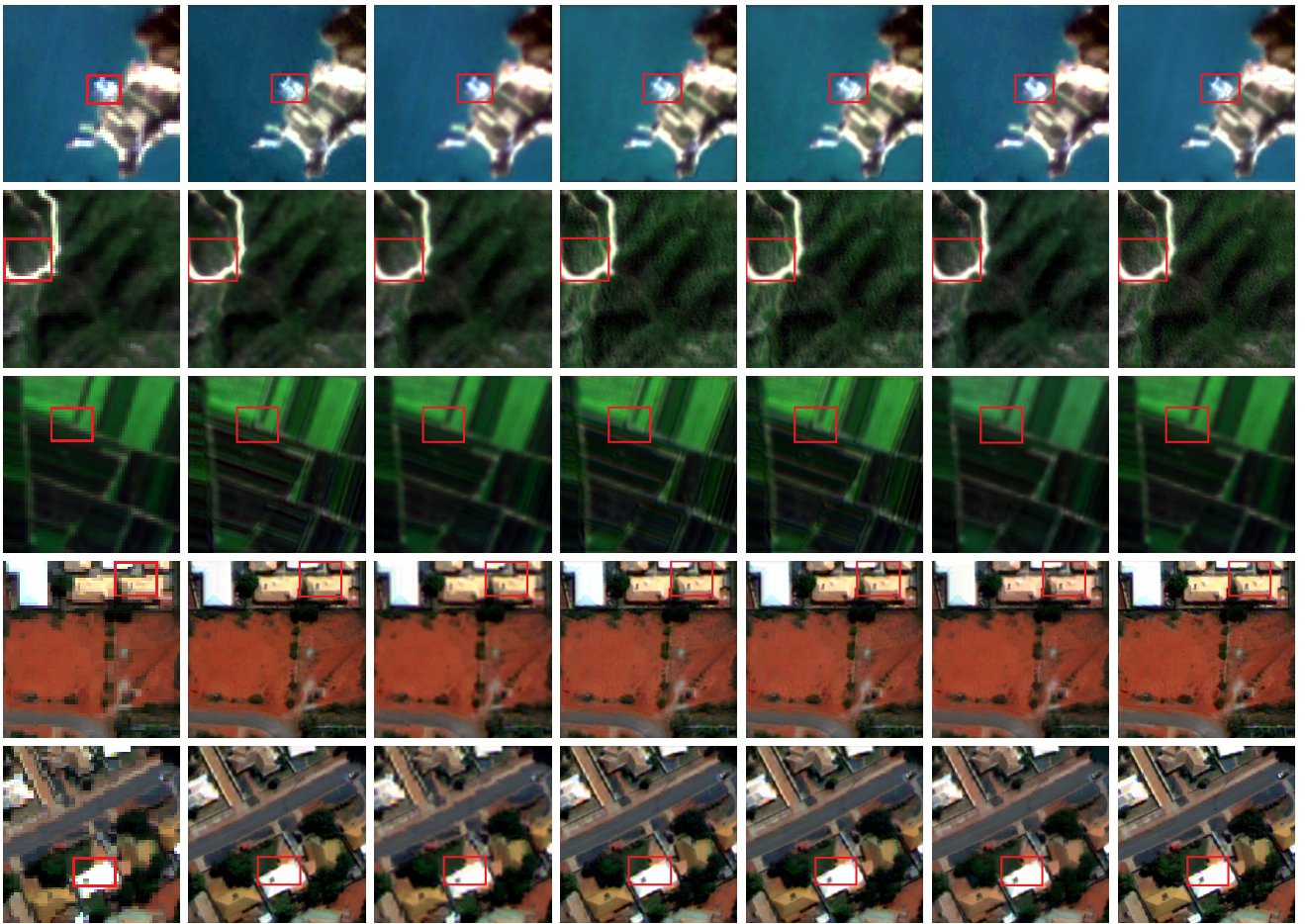


Fig. 10. Full-resolution visualization results generated by different DL-based pan-sharpening methods (left to right: MS image, PNN [9], PANNet [32], MSDCNN [57], FusionNet [33], ADKNet [58] and Ours). The first three rows are sampled from the Gaofen1 dataset, while the last two rows are from the WorldView-4 dataset.

Figure 9, we can see from the MAE images that the super-resolution images obtained from our method are the closest to the reference image, which verifies the quantitative results on the super-resolution task.

#### H. Pan-sharpening on full-resolution scene

**Quantitative comparison.** In order to demonstrate the real-world application value, we also conduct experiments on full-resolution scenes obtained from the WorldView-4 satellite. A quantitative comparison between promising DL-based methods and our framework is presented in the following Table VIII. The lower  $D_\lambda$ ,  $D_s$ , and the higher QNR correspond to the better image quality, where the best results are highlighted in bold. As can be seen obviously, our methods overpass other competitive pan-sharpening methods, which demonstrate excellent ability in real-world application.

**Qualitative comparison.** We further perform a full-resolution visualization on the Gaofen1 and WorldView-4 datasets. The qualitative results are shown in Figure 10. From the red box, we can observe that our method outperforms other methods in both spectral fidelity and spatial resolution. Especially, from the third row of Figure 10, we also find that our method can

well solve the artefacts and texture blurring problem caused by the misalignment between PAN and MS images, which benefits from the fact that our method does not require PAN images in practical applications. The above results demonstrate the effectiveness and universality of our method.

## VI. CONCLUSION

In this work, we formulated a new representation of the spatial details and proposed a novel memory-based network called MSDN to generate the required spatial details instead of obtaining them from PAN images. To model it, we decomposed the MSDN into two subnetworks: a memory-controlled subnetwork and a weighted coefficient subnetwork. In the memory-controlled subnetwork, we encoded the MS features in the memory encoder to query the corresponding spatial details from the memory bank and then obtained the spatial features through the memory decoder. As for the weighted coefficient subnetwork, we utilized channel attention to predict the weighted features. The two subnetworks are tightly coupled and generate the required spatial details. We also conducted an MSDN-based pan-sharpening framework to evaluate its effectiveness. The framework was easy to extend and can be trained in an end-to-end manner. The results of

additional ablation studies support the effectiveness of the proposed components. In addition, our method outperforms other conventional and state-of-the-art methods in both reduced- and full-resolution experiments on GF1 and WorldView-4 datasets, indicating the good generalisation of the proposed method. For future work, we will explore the method of utilizing PAN images to directly generate pan-sharpening images and embed it into our proposed framework. We believe our method will be useful in real-world applications.

## REFERENCES

- [1] X. Liu, L. Li, F. Liu, B. Hou, S. Yang, and L. Jiao, "Gafnet: Group attention fusion network for pan and ms image high-resolution classification," *IEEE Transactions on Cybernetics*, vol. 52, no. 10, pp. 10556–10569, 2021. **1**
- [2] X. Lu, Y. Yuan, and X. Zheng, "Joint dictionary learning for multispectral change detection," *IEEE transactions on cybernetics*, vol. 47, no. 4, pp. 884–897, 2016. **1**
- [3] X. Wei and M. Yuan, "Adversarial pan-sharpening attacks for object detection in remote sensing," *Pattern Recognition*, vol. 139, p. 109466, 2023. **1**
- [4] G. Vivone, M. Dalla Mura, A. Garzelli, R. Restaino, G. Scarpa, M. O. Ulfarsson, L. Alparone, and J. Chanussot, "A new benchmark based on recent advances in multispectral pansharpening: Revisiting pansharpening with classical and emerging pansharpening methods," *IEEE Geoscience and Remote Sensing Magazine*, vol. 9, no. 1, pp. 53–81, 2020. **1, 2**
- [5] J. Feng, Q. Jiang, C.-H. Tseng, X. Jin, L. Liu, W. Zhou, and S. Yao, "A deep multitask convolutional neural network for remote sensing image super-resolution and colorization," *IEEE Transactions on Geoscience and Remote Sensing*, vol. 60, pp. 1–15, 2022. **1**
- [6] L. Alparone, L. Wald, J. Chanussot, C. Thomas, P. Gamba, and L. M. Bruce, "Comparison of pansharpening algorithms: Outcome of the 2006 grs-s data-fusion contest," *IEEE Transactions on Geoscience and Remote Sensing*, vol. 45, no. 10, pp. 3012–3021, 2007. **1**
- [7] L. Zhang, H. Shen, W. Gong, and H. Zhang, "Adjustable model-based fusion method for multispectral and panchromatic images," *IEEE Transactions on Systems, Man, and Cybernetics, Part B (Cybernetics)*, vol. 42, no. 6, pp. 1693–1704, 2012. **1**
- [8] X. Zhou, J. Liu, S. Liu, L. Cao, Q. Zhou, and H. Huang, "A gihs-based spectral preservation fusion method for remote sensing images using edge restored spectral modulation," *ISPRS Journal of Photogrammetry and Remote Sensing*, vol. 88, pp. 16–27, 2014. **1**
- [9] G. Masi, D. Cozzolino, L. Verdoliva, and G. Scarpa, "Pansharpening by convolutional neural networks," *Remote Sensing*, vol. 8, no. 7, p. 594, 2016. **1, 7, 9, 10**
- [10] Y. Wei, Q. Yuan, H. Shen, and L. Zhang, "Boosting the accuracy of multispectral image pansharpening by learning a deep residual network," *IEEE Geoscience and Remote Sensing Letters*, vol. 14, no. 10, pp. 1795–1799, 2017. **1**
- [11] Y. Zhang, C. Liu, M. Sun, and Y. Ou, "Pan-sharpening using an efficient bidirectional pyramid network," *IEEE Transactions on Geoscience and Remote Sensing*, vol. 57, no. 8, pp. 5549–5563, 2019. **1**
- [12] J. Cai and B. Huang, "Super-resolution-guided progressive pansharpening based on a deep convolutional neural network," *IEEE Transactions on Geoscience and Remote Sensing*, vol. 59, no. 6, pp. 5206–5220, 2020. **1**
- [13] Y. Zheng, J. Li, Y. Li, J. Guo, X. Wu, and J. Chanussot, "Hyperspectral pansharpening using deep prior and dual attention residual network," *IEEE transactions on geoscience and remote sensing*, vol. 58, no. 11, pp. 8059–8076, 2020. **1**
- [14] T. Wang, F. Fang, H. Zheng, and G. Zhang, "Frmnet: Framelet-based multilevel network for pansharpening," *IEEE Transactions on Cybernetics*, 2021. **1**
- [15] W. G. C. Bandara, J. M. J. Valanarasu, and V. M. Patel, "Hyperspectral pansharpening based on improved deep image prior and residual reconstruction," *IEEE Transactions on Geoscience and Remote Sensing*, vol. 60, pp. 1–16, 2021. **1**
- [16] M. Zhou, J. Huang, F. Zhao, and D. Hong, "Modality-aware feature integration for pan-sharpening," *IEEE Transactions on Geoscience and Remote Sensing*, 2022. **1**
- [17] M. Zhou, J. Huang, X. Fu, F. Zhao, and D. Hong, "Effective pansharpening by multiscale invertible neural network and heterogeneous task distilling," *IEEE Transactions on Geoscience and Remote Sensing*, vol. 60, pp. 1–14, 2022. **1**
- [18] Q. Poterek, P.-A. Herrault, G. Skupinski, and D. Sheeren, "Deep learning for automatic colorization of legacy grayscale aerial photographs," *IEEE Journal of Selected Topics in Applied Earth Observations and Remote Sensing*, vol. 13, pp. 2899–2915, 2020. **1**
- [19] L. Liu, Q. Jiang, X. Jin, J. Feng, R. Wang, H. Liao, S.-J. Lee, and S. Yao, "Casr-net: A color-aware super-resolution network for panchromatic image," *Engineering Applications of Artificial Intelligence*, vol. 114, p. 105084, 2022. **1**
- [20] C. Dong, C. C. Loy, K. He, and X. Tang, "Image super-resolution using deep convolutional networks," *IEEE transactions on pattern analysis and machine intelligence*, vol. 38, no. 2, pp. 295–307, 2015. **1, 7, 8, 9**
- [21] J. M. Haut, M. E. Paoletti, R. Fernández-Beltrán, J. Plaza, A. Plaza, and J. Li, "Remote sensing single-image superresolution based on a deep compendium model," *IEEE Geoscience and Remote Sensing Letters*, vol. 16, no. 9, pp. 1432–1436, 2019. **1, 7, 8, 9**
- [22] S. Lei and Z. Shi, "Hybrid-scale self-similarity exploitation for remote sensing image super-resolution," *IEEE Transactions on Geoscience and Remote Sensing*, vol. 60, pp. 1–10, 2021. **1, 7, 8, 9**
- [23] P. Chavez, S. C. Sides, J. A. Anderson *et al.*, "Comparison of three different methods to merge multiresolution and multispectral data-landsat tm and spot panchromatic," *Photogrammetric Engineering and Remote Sensing*, vol. 57, no. 3, pp. 295–303, 1991. **2, 3**
- [24] J. Liu, "Smoothing filter-based intensity modulation: A spectral preserve image fusion technique for improving spatial details," *International Journal of Remote Sensing*, vol. 21, no. 18, pp. 3461–3472, 2000. **2, 7, 9**
- [25] J. Weston, S. Chopra, and A. Bordes, "Memory networks," in *3rd International Conference on Learning Representations, ICLR 2015*, 2015. **2, 3**
- [26] G. Vivone, L. Alparone, J. Chanussot, M. Dalla Mura, A. Garzelli, G. A. Licciardi, R. Restaino, and L. Wald, "A critical comparison among pansharpening algorithms," *IEEE Transactions on Geoscience and Remote Sensing*, vol. 53, no. 5, pp. 2565–2586, 2014. **2**
- [27] A. Garzelli, F. Nencini, and L. Capobianco, "Optimal mmse pan sharpening of very high resolution multispectral images," *IEEE Transactions on Geoscience and Remote Sensing*, vol. 46, no. 1, pp. 228–236, 2007. **2**
- [28] L. Wald, "Quality of high resolution synthesised images: Is there a simple criterion?" in *Third conference Fusion of Earth data: merging point measurements, raster maps and remotely sensed images*. SEE/URISCA, 2000, pp. 99–103. **2, 7**
- [29] B. Aiazzi, L. Alparone, S. Baronti, and A. Garzelli, "Context-driven fusion of high spatial and spectral resolution images based on oversampled multiresolution analysis," *IEEE Transactions on geoscience and remote sensing*, vol. 40, no. 10, pp. 2300–2312, 2002. **2, 7, 9**
- [30] X. Otazu, M. González-Audicana, O. Fors, and J. Núñez, "Introduction of sensor spectral response into image fusion methods. application to wavelet-based methods," *IEEE Transactions on Geoscience and Remote Sensing*, vol. 43, no. 10, pp. 2376–2385, 2005. **2**
- [31] L. He, Y. Rao, J. Li, J. Chanussot, A. Plaza, J. Zhu, and B. Li, "Pansharpening via detail injection based convolutional neural networks," *IEEE Journal of Selected Topics in Applied Earth Observations and Remote Sensing*, vol. 12, no. 4, pp. 1188–1204, 2019. **2**
- [32] J. Yang, X. Fu, Y. Hu, Y. Huang, X. Ding, and J. Paisley, "Pannet: A deep network architecture for pan-sharpening," in *Proceedings of the IEEE international conference on computer vision*, 2017, pp. 5449–5457. **3, 4, 7, 9, 10**
- [33] L.-J. Deng, G. Vivone, C. Jin, and J. Chanussot, "Detail injection-based deep convolutional neural networks for pansharpening," *IEEE Transactions on Geoscience and Remote Sensing*, vol. 59, no. 8, pp. 6995–7010, 2021. **3, 5, 7, 9, 10**
- [34] Z. Xiang, L. Xiao, J. Yang, W. Liao, and W. Philips, "Detail-injection-model-inspired deep fusion network for pansharpening," *IEEE Transactions on Geoscience and Remote Sensing*, vol. 60, pp. 1–15, 2022. **3**
- [35] H. Deng, Y. Hua, T. Song, Z. Zhang, Z. Xue, R. Ma, N. Robertson, and H. Guan, "Object guided external memory network for video object detection," in *Proceedings of the IEEE/CVF International Conference on Computer Vision*, 2019, pp. 6678–6687. **3**
- [36] H. Xie, H. Yao, S. Zhou, S. Zhang, and W. Sun, "Efficient regional memory network for video object segmentation," in *Proceedings of the IEEE/CVF Conference on Computer Vision and Pattern Recognition (CVPR)*, June 2021, pp. 1286–1295. **3**

- [37] B. Ji and A. Yao, "Multi-scale memory-based video deblurring," in *Proceedings of the IEEE/CVF Conference on Computer Vision and Pattern Recognition (CVPR)*, June 2022, pp. 1919–1928. [3](#)
- [38] K. Yan, M. Zhou, L. Zhang, and C. Xie, "Memory-augmented model-driven network for pansharpening," in *European Conference on Computer Vision*. Springer, 2022, pp. 306–322. [3](#)
- [39] X. X. Zhu and R. Bamler, "A sparse image fusion algorithm with application to pan-sharpening," *IEEE transactions on geoscience and remote sensing*, vol. 51, no. 5, pp. 2827–2836, 2012. [3](#)
- [40] S. Maeda, "Image super-resolution with deep dictionary," in *European Conference on Computer Vision*. Springer, 2022, pp. 464–480. [3](#)
- [41] K. He, X. Zhang, S. Ren, and J. Sun, "Delving deep into rectifiers: Surpassing human-level performance on imagenet classification," in *Proceedings of the IEEE international conference on computer vision*, 2015, pp. 1026–1034. [4](#), [5](#)
- [42] J. Yang, J. Wright, T. S. Huang, and Y. Ma, "Image super-resolution via sparse representation," *IEEE transactions on image processing*, vol. 19, no. 11, pp. 2861–2873, 2010. [4](#)
- [43] O. Ronneberger, P. Fischer, and T. Brox, "U-net: Convolutional networks for biomedical image segmentation," in *International Conference on Medical image computing and computer-assisted intervention*. Springer, 2015, pp. 234–241. [5](#)
- [44] X. Meng, Y. Xiong, F. Shao, H. Shen, W. Sun, G. Yang, Q. Yuan, R. Fu, and H. Zhang, "A large-scale benchmark data set for evaluating pansharpening performance: Overview and implementation," *IEEE Geoscience and Remote Sensing Magazine*, vol. 9, no. 1, pp. 18–52, 2020. [6](#)
- [45] L. Wald, T. Ranchin, and M. Mangolini, "Fusion of satellite images of different spatial resolutions: Assessing the quality of resulting images," *Photogrammetric engineering and remote sensing*, vol. 63, no. 6, pp. 691–699, 1997. [6](#)
- [46] J. Zhou, D. L. Civco, and J. Silander, "A wavelet transform method to merge landsat tm and spot panchromatic data," *International journal of remote sensing*, vol. 19, no. 4, pp. 743–757, 1998. [7](#)
- [47] R. H. Yuhas, A. F. Goetz, and J. W. Boardman, "Discrimination among semi-arid landscape endmembers using the spectral angle mapper (sam) algorithm," in *JPL, Summaries of the Third Annual JPL Airborne Geoscience Workshop. Volume 1: AVIRIS Workshop*, 1992. [7](#)
- [48] L. Alparone, S. Baronti, A. Garzelli, and F. Nencini, "A global quality measurement of pan-sharpened multispectral imagery," *IEEE Geoscience and Remote Sensing Letters*, vol. 1, no. 4, pp. 313–317, 2004. [7](#)
- [49] L. Alparone, B. Aiazzi, S. Baronti, A. Garzelli, F. Nencini, and M. Selva, "Multispectral and panchromatic data fusion assessment without reference," *Photogrammetric Engineering & Remote Sensing*, vol. 74, no. 2, pp. 193–200, 2008. [7](#)
- [50] A. Paszke, S. Gross, F. Massa, A. Lerer, J. Bradbury, G. Chanan, T. Killeen, Z. Lin, N. Gimelshein, L. Antiga *et al.*, "Pytorch: An imperative style, high-performance deep learning library," *Advances in neural information processing systems*, vol. 32, 2019. [7](#)
- [51] D. P. Kingma and J. Ba, "Adam: A method for stochastic optimization," *arXiv preprint arXiv:1412.6980*, 2014. [7](#)
- [52] C. A. Laben and B. V. Brower, "Process for enhancing the spatial resolution of multispectral imagery using pan-sharpening," Jan. 4 2000, uS Patent 6,011,875. [7](#), [9](#)
- [53] B. Aiazzi, S. Baronti, and M. Selva, "Improving component substitution pansharpening through multivariate regression of ms + pan data," *IEEE Transactions on Geoscience and Remote Sensing*, vol. 45, no. 10, pp. 3230–3239, 2007. [7](#), [9](#)
- [54] A. R. Gillespie, A. B. Kahle, and R. E. Walker, "Color enhancement of highly correlated images. ii. channel ratio and "chromaticity" transformation techniques," *Remote Sensing of Environment*, vol. 22, no. 3, pp. 343–365, 1987. [7](#), [9](#)
- [55] W. Liao, X. Huang, F. Van Coillie, G. Thoonen, A. Pižurica, P. Scheunders, and W. Philips, "Two-stage fusion of thermal hyperspectral and visible rgb image by pca and guided filter," in *2015 7th Workshop on Hyperspectral Image and Signal Processing: Evolution in Remote Sensing (WHISPERS)*, 2015, pp. 1–4. [7](#), [9](#)
- [56] J. Lee and C. Lee, "Fast and efficient panchromatic sharpening," *IEEE Transactions on Geoscience and Remote Sensing*, vol. 48, no. 1, pp. 155–163, 2009. [7](#), [9](#)
- [57] Q. Yuan, Y. Wei, X. Meng, H. Shen, and L. Zhang, "A multiscale and multidepth convolutional neural network for remote sensing imagery pan-sharpening," *IEEE Journal of Selected Topics in Applied Earth Observations and Remote Sensing*, vol. 11, no. 3, pp. 978–989, 2018. [7](#), [9](#), [10](#)
- [58] S. Peng, L.-J. Deng, J.-F. Hu, and Y. Zhuo, "Source-adaptive discriminative kernels based network for remote sensing pansharpening," in *Proceedings of the Thirty-First International Joint Conference on Artificial Intelligence, IJCAI-22*, L. D. Raedt, Ed. International Joint Conferences on Artificial Intelligence Organization, 7 2022, pp. 1283–1289, main Track. [Online]. Available: <https://doi.org/10.24963/ijcai.2022/179> [7](#), [9](#), [10](#)
- [59] J. Kim, J. K. Lee, and K. M. Lee, "Accurate image super-resolution using very deep convolutional networks," in *Proceedings of the IEEE conference on computer vision and pattern recognition*, 2016, pp. 1646–1654. [7](#), [8](#), [9](#)
- [60] S. Lei, Z. Shi, and Z. Zou, "Super-resolution for remote sensing images via local-global combined network," *IEEE Geoscience and Remote Sensing Letters*, vol. 14, no. 8, pp. 1243–1247, 2017. [7](#), [8](#), [9](#)